

HST/NICMOS IMAGING POLARIMETRY OF PROTO-PLANETARY NEBULAE: PROBING OF THE DUST SHELL STRUCTURE VIA POLARIZED LIGHT

TOSHIYA UETA^{1,2,3}, KOJI MURAKAWA^{4,5}, MARGARET MEIXNER⁶

(Received Aug 24, 2004; Revised Oct 13, Nov 12, 2004; Accepted Nov 18, 2004)
To be published in the Astronomical Journal

ABSTRACT

Using NICMOS on *HST*, we have performed imaging polarimetry of proto-planetary nebulae. Our objective is to study the structure of *optically thin* circumstellar shells of post-asymptotic giant branch stars by separating dust-scattered, linearly polarized star light from unpolarized direct star light. This unique technique allows us to probe faint reflection nebulae around the bright central star, which can be buried under the point-spread-function of the central star in conventional imaging. Our observations and archival search have yielded polarimetric images for five sources: *IRAS* 07134+1005 (HD 56126), *IRAS* 06530–0213, *IRAS* 04296+3429, *IRAS* (Z)02229+6208, and *IRAS* 16594–4656. These images have revealed the circumstellar dust distribution in an unprecedented detail via polarized intensity maps, providing a basis to understand the 3-D structure of these dust shells. We have observationally confirmed the presence of the inner cavity caused by the cessation of AGB mass loss and the internal shell structures which is strongly tied to the progenitor star's mass loss history on the AGB. We have also found that equatorial enhancement in these circumstellar shells comes with various degrees of contrast, suggesting a range of optical depths in these optically thin shells. Our data support the interpretation that the dichotomy of PPN morphologies is due primarily to differences in optical depth and secondary to the inclination effect. The polarization maps reveal a range of inclination angles for these optically thin reflection nebulae, dispelling the notion that elliptical nebulae are pole-on bipolar nebulae.

Subject headings: circumstellar matter — stars: AGB and post-AGB — stars: mass loss — planetary nebulae: general — reflection nebulae

1. INTRODUCTION

The proto-planetary nebula (PPN) phase is a relatively short ($\sim 10^3$ years) stage of stellar evolution for low to intermediate initial mass ($\sim 0.8 - 8 M_{\odot}$) stars between the asymptotic giant branch (AGB) and planetary nebula (PN) phases (e.g., Kwok 1993; Van Winckel 2003). During the PPN phase the post-AGB central star increases its surface temperature from a few to a few tens of 10^3 K, while the circumstellar dust shell - created by the AGB mass loss and physically detached from the central star at the end of the AGB phase - simply coasts away from the central star. Therefore, PPNs are important stellar objects in which to investigate the nature of dusty mass loss during the AGB phase, because the most pristine history of AGB mass loss is imprinted and preserved in their density distribution.

The AGB mass loss history can provide crucial clues for the shell structure formation. While the circumstellar shells of AGB stars initially assume spherically symmetric shape when they are formed, they seem to develop largely axisymmetric structure by the time the AGB mass loss is terminated (e.g., Balick & Frank 2002 for a review). Meanwhile, the AGB mass loss history can also yield information about the internal evolution of the central star. AGB mass loss may show temporal variations due to the alternative burning of hydrogen and helium in two distinct layers via the mechanism called ther-

mal pulsation (Iben 1981), while a sudden enhancement of mass loss near the end of the AGB phase - the so-called superwind (Renzini 1981; Iben & Renzini 1983) - may remove almost the entire surface layer from the star terminating the AGB evolution. Thus, the AGB mass loss history is strongly linked to both the internal and external evolution of the central star, and the effects of AGB mass loss can manifest themselves in the density distribution in the PPN dust shells.

The density distribution in PPNs can be observationally studied in two ways: either directly via thermal dust emission arising from the shells or indirectly via scattered light through the dusty shells. PPN imaging surveys were conducted using both methods, and the combined results suggested that PPNs were intrinsically axisymmetric due to equatorially-enhanced mass loss near the end of the AGB phase, which probably coincides with the superwind phase (Meixner et al. 1999; Ueta, Meixner, & Bobrowsky 2000). These surveys also found a morphological dichotomy among PPNs, showing one-to-one correspondence between the mid-IR and optical morphologies: an optical bipolar reflection nebula is always found with a mid-IR emission nebula of a single core surrounded by an elliptical low-emission halo (DUPLEX-core/elliptical PPNs), while an optical elliptical nebula is usually associated with a mid-IR emission nebula harboring two emission peaks as evidence for limb-brightened edge-on dust torus (SOLE-toroidal PPNs). Subsequent radiative transfer calculations showed that the optical depth of the shell would play a more important role in determining the morphology of the shell than the inclination effect (Meixner et al. 2002; Ueta & Meixner 2003).

In both morphological cases, the source of axisymmetric structure is an equatorial density enhancement present in the innermost regions of the shell. Hence, the AGB mass loss history represented by this part of the shell holds

¹ Royal Observatory of Belgium, Ringlaan, 3, B-1180, Brussels, Belgium

² Current Address: NASA Ames Research Center/SOFIA, Mail Stop 211-3, Moffett Field, CA 94035, USA; tueta@mail.sofia.usra.edu

³ NRC Research Associate

⁴ Subaru Telescope, National Astronomical Observatory of Japan, 650 North A'ohoku Place Hilo, HI 96720, USA; murakawa@subaru.naoj.org

⁵ Current Address: ASTRON, P.O. Box 2, 7990 AA, Dwingeloo The Netherlands

⁶ Space Telescope Science Institute, 3700 San Martin Drive, Baltimore, MD 21218, USA; meixner@stsci.edu

the critical piece of information to enhance our understanding of mass loss processes. Taking advantage of their optically thin nature, SOLE-toroidal PPNs have been studied by high-resolution imaging of thermal dust emission at mid-IR in order to reveal the density distribution in these shells (Dayal et al. 1998; Ueta et al. 2001; Kwok, Volk, & Hrivnak 2002; Gledhill & Yates 2003). However, such studies have been difficult to perform at sufficient spatial resolution because of the diffraction-limited nature of the mid-IR imaging and the intrinsically compact nature of PPNs.

In this paper, we use near-IR imaging polarimetry to investigate the structure of five SOLE-toroidal PPN: *IRAS* 07134+1005 (HD 56126), *IRAS* 06530–0213, *IRAS* 04296+3429, *IRAS* (Z)02229+6208, and *IRAS* 16594–4656. Below, we describe the technique of near-IR imaging polarimetry and motivate our use of it in this study (§2) and outline our observational procedure and data processing steps (§3). In §4, we present the results, and discuss the individual sources in §5. We then discuss some of the implications of the results (§6) and summarize the conclusions (§7).

2. IMAGING POLARIMETRY OF PPNs

Gledhill et al. (2001) used near-IR imaging polarimetry as an alternative technique to directly capture the structure of the PPN dust shells. The imaging polarimetry can separate dust-scattered light (as the linearly polarized component) from direct star light (as the unpolarized component). Hence, one can easily detect faint, dust-scattered light from PPNs that is otherwise buried beneath the dominant point-spread-function (PSF) of the central star: the PPN structure can thus be revealed as in the mid-IR imaging, but at one order better resolution in the near-IR. For example, the shell structure of HD 235858 (*IRAS* 22272+5435), which was not fully resolved at mid-IR until observed with the 10 m Keck telescope (Ueta et al. 2001), was resolved by near-IR imaging polarimetry with the 4 m UKIRT (Gledhill et al. 2001). Therefore, we performed imaging polarimetry with the Hubble Space Telescope (*HST*) to investigate the structure of very compact PPNs by exploiting the unique ability of this novel observing method and the high resolution capabilities of the telescope.

Polarimetric characteristics of astronomical objects can be obtained by means of the Stokes parameters, (I , Q , U), which are computed from the measurements of the beam intensity passing through linear polarizing elements. The near-IR camera and multiple object spectrometer (NICMOS; Malhotra et al. 2002) on *HST* is equipped with three polarizers, and the Stokes parameters can be derived by a matrix conversion method that is elucidated by Sparks & Axon (1999) and Hines, Schmidt, & Schneider (2000). Using the Stokes I (the total intensity) along with the Stokes Q and U , we can then express the intensity of linearly polarized light, I_p , the polarization strength, P , and the polarization PA, θ .

However, one must exercise caution when computing P because I can be affected by the (unpolarized) PSF of the central source (e.g., Gledhill & Takami 2001). The PSF of the central star can (1) accompany enormous spider structures that spatially affect the detectability of the circumstellar shell and (2) induce very large I with respect to potentially small I_p , especially when the optical depth of the surrounding matter is low. In such cases, the PSF contribution, I_{psf} , has to be removed from I to obtain the *PSF-corrected* polarization strength, P_{corr} :

$$P_{\text{corr}} = \frac{I_p}{I - I_{\text{psf}}}. \quad (1)$$

In order for the PSF correction to be effective, PSF reference observations must be carefully designed. The PSF observations should achieve a similar S/N to the source observations, yielding spatially and quantitatively equivalent PSF structures. The removal of the PSF effect is difficult even with good PSF reference data, since there is no way to know *a priori* how much matter exists along the line of sight in front of the central source. The scaling of the PSF reference data with respect to the target data would always be a problem, and hence, P as a ratio of I_p to I (irrespective of the PSF correction) should be considered to roughly define the *lower* limit. In the following, we refer to P_{corr} as P . On the contrary, I_p and θ can be extracted even from the PSF-affected data because these quantities depend only on Q and U which are free from the unpolarized component by definition. Therefore, we will make use of the I_p maps in addition to the P maps to investigate the shell structure in PPNs.

3. OBSERVATIONS AND DATA REDUCTION

3.1. Observations

We obtained high-resolution near-IR polarimetric data from four PPNs using NICMOS on-board *HST* through a general observer (GO) program 9377 (PI: T. Ueta) during Cycle 11, after the NICMOS cooling system (NCS) was installed during the servicing mission 3B (SM3B). We selected the target sources (*IRAS* 07134+1005, *IRAS* 06530–0213, *IRAS* 04296+3429, and *IRAS* [Z]02229+6208⁷) based on their morphological classification in a previous WFPC2 survey (Ueta, Meixner, & Bobrowsky 2000): they are all SOLE-toroidal PPNs. We observed our targets with Camera 1 (NIC1), which provides $11'' \times 11''$ field of view at $0''.043 \text{ pixel}^{-1}$ scale, and short wavelength polarizers (POL0S, POL120S, and POL240S, covering 0.8 to 1.3 μm). We used the MULTIACCUM (non-destructive readout) mode to recover information in saturated pixels from unsaturated readouts.

To remove the effects of bad pixels and improve the spatial sampling of the PSF, we employed the dithering technique and observed each source at five or four dithering positions (i.e., four-point spiral pattern with or without the pattern center) with offsets by non-integer pixels. At each dither position we took images using all three polarizers, allocating equal amount of exposure time to each polarizer. The observations were designed this way to make the visits as efficient as possible. However, taking multiple exposures at each dither position can cause a problem particularly when a wide dynamic range has to be covered, since image persistence due to very bright parts of the source (the central star, in our case) may leave photon persistence that can affect the subsequent exposures (e.g., Dickinson et al. 2002). To reduce the effect of persistence, we took two 5.158 sec BLANK exposures after each exposure with a polarizer.

In addition to the four target sources, we also obtained data from a PSF reference star, HD 12088, since we concluded from our previous experience with WFPC2 that the best way to reduce the PSF effects from *HST* data was to use observed PSF data (Ueta, Meixner, & Bobrowsky 2000). This high proper-motion star was selected as a PSF reference because (1) most unpolarized stars are known to be high proper-

⁷ Hereafter, we refer to each object by the RA part of the *IRAS* designation. The prefix “Z” for *IRAS* 02229 is given by Hrivnak & Kwok (1999) due to the fact that the source was found in the Faint Source Reject File in the *IRAS* Faint Source Survey.

TABLE 1
LOG OF HST/NICMOS OBSERVATIONS

Source	Date	FILTER ^a	SAMP_SEQ	NSAMP	DITHER		EXPTIME ^b (sec)	ORIENTAT ^c (deg)	Ref.
					PATTERN	NPTS			
New Data									
IRAS 07134+1005	2003 Mar 29	POL-S	STEP8	19	SPIRAL	5	519.5079	-129.432	
IRAS 06530-0213	2003 Mar 29	POL-S	STEP8	19	SPIRAL	5	519.5079	-131.793	
IRAS 04296+3429	2003 Mar 28	POL-S	STEP8	19	SPIRAL	5	519.5079	-149.313	
IRAS (Z)02229+6208 ^d	2003 Mar 28	POL-S	STEP8	16	SPIRAL	4	319.6832	169.035	
HD 12088 ^e	2003 Mar 28	POL-S	STEP1	19	SPIRAL	5	79.7868	162.51	
Archived Data									
IRAS 16594-4656	1998 May 2	POL-L	STEP32	17	SPIRAL	3	863.8767	78.9531	2
BD +32° 3739 ^f	1997 Sep 1	POL-L	STEP1	9	NONE	...	41.86784	-93.5733	1
	2002 Sep 9	POL-S	SCAMRR	9	SPIRAL	4	12.992	-108.88	
	2003 Jun 8	POL-S	SCAMRR	9	SPIRAL	4	12.992	1.32	

REFERENCES. — 1. Hines, Schmidt, & Schneider (2000), 2. Su et al. (2003)

^aPOL-S: short wavelength polarizers (POL0S, POL120S, and POL240S); POL-L: long wavelength polarizers (POL0L, POL120L, and POL240L)

^bTotal exposure time per polarizer.

^cThe ORIENTAT header parameter refers to PA of the image +y axis (degrees E of N).

^dThe “Z” prefix in the IRAS designation is given to indicate the fact that this object was found in the Faint Source Reject File in the IRAS Faint Source Survey (Hrivnak & Kwok 1999).

^ePSF standard for our target sources.

^fPSF (and photometric) standard for the archived data.

motion stars and (2) this star lies in the continuous viewing zone (CVZ) and can be observed in the same orbit as one of the target sources that is also in the CVZ without spending an additional orbit just for PSF observations. The same instrumental set-up was used for the PSF reference observations. We summarize the observing parameters in Table 1.

We are interested in the morphologies of the circumstellar shells revealed by the dust-scattered, polarized light. Although polarimetric data have been acquired from evolved stars with NICMOS in the past, no study has been done to extract the spatial information from the data by alleviating the PSF effects of the bright central star. Therefore, we have analyzed all the archived NICMOS polarimetric data obtained from evolved stars (mostly done with NIC2) to study the shell structure. Here, we included data from a PPN, IRAS 16594-4656, whose I_p map provides more spatial information of the shell structure than previously reported (Su et al. 2003). IRAS 16594-4656 was originally observed in a GO program 7840 (PI: S. Kwok), in which Camera 2 (NIC2; $19''.2 \times 19''.2$ field of view at $0''.075 \text{ pixel}^{-1}$ scale) and long wavelength polarizers (POL0L, POL120L, and POL240L, covering 1.9 to $2.1 \mu\text{m}$) were used with the three-point spiral dither pattern. Table 1 also shows observing parameters for the additional sources.

3.2. Data Reduction

We used the standard set of NICMOS calibration programs provided in the latest version (Version 3.1) of IRAF/STSDAS⁸ at the time of data reduction. The CALNICA calibration routines in STSDAS perform zero-read signal correction, bias subtraction, dark subtraction, detector non-linearity correction, flat-field correction, and flux calibration. After pipeline calibration, we realized that our data were

affected by the “pedestal effect”, a variable quadrant bias, and the “Mr. Staypuft”, the amplifier ringing and streaking due to bright targets (Dickinson et al. 2002). The pedestal effect was removed by first manually inserting the STSDAS task *biaseq* in the middle of the CALNICA processes (before flat-fielding) and then employing the STSDAS task *pedsub* after the CALNICA processes. The former removes the non-linear components of the bias drift, while the latter takes care of the linear components. To remove the “Mr. Staypuft” anomaly, we applied “undopuft” IDL routines provided by the STScI NICMOS group to the raw data before using any of the CALNICA routines. Any remaining stripes along the fast read-out direction associated with “Mr. Staypuft” were subtracted by extracting the anomalous stripes from the block-averaged blank sky.

The calibrated, anomaly-cleaned frames of dithered images were then combined into a single image by applying the variable-pixel linear reconstruction algorithm (the STSDAS package *dither*, Version 2.0; Koekemoer et al. 2002). This method would interlace (“drizzle”) each pixel in multi-point dithered frames according to the statistical significance of each pixel. The drizzled images were sub-pixelized by a factor of 2 during the process: the reduced images would have pixel scales of $0''.0215 \text{ pixel}^{-1}$ (NIC1) and $0''.0375 \text{ pixel}^{-1}$ (NIC2). Cosmic-rays were also removed by the drizzling algorithm.

The NICMOS arrays are slightly tilted with respect to the focal plane, and thus the NICMOS pixel scales along the two spatial axes of each camera are not identical. Although its effect is small, pixels have to be properly rectified to accurately determine the orientation of the polarization vectors. Since the geometric distortion parameters have been found to be identical before and after SM3B, we simply applied the geometrical transformation within the drizzle process, using the geometric distortion coefficients provided by the STScI NICMOS group.

⁸ STSDAS is a product of the Space Telescope Science Institute, which is operated by AURA for NASA

TABLE 2
PHOTOMETRIC AND POLARIMETRIC CALIBRATION PARAMETERS

Polarizer	PHOTFNU (Jy sec DN^{-1})		t_k	
	Pre-SM3B	Post-SM3B	Pre-SM3B	Post-SM3B
POL0S	6.996 E-06	4.31 E-06	0.7766	0.7760
POL120S	6.912 E-06	4.19 E-06	0.5946	0.5935
POL240S	6.914 E-06	4.15 E-06	0.7169	0.7181
POL0L	7.626 E-06	6.17 E-06	0.7313	0.8774
POL120L	7.530 E-06	6.10 E-06	0.6288	0.8381
POL240L	7.517 E-06	6.04 E-06	0.8738	0.9667

3.3. Derivation of the Stokes Parameters

At the end of the processes described above, images would have units of the default count rate for *HST* data (DN sec^{-1} ; “DN” = data number). These count rates can be translated into appropriate physical units by means of photometric conversion factors, PHOTFLAM and PHOTFNU, before the Stokes parameters are derived from the data. However, these factors depend on the actual detector sensitivities, which were altered after the NCS installation due to the 15 K raise of the NICMOS detector operating temperature. Since post-SM3B photometric conversion factors for the polarizers were not available at the time of our analysis, we estimated them following the method described below.

First we retrieved archived NICMOS calibration data of an unpolarized standard star, BD+32°3739, from CAL programs executed before and after SM3B (PIDs: 7692, 7958, and 9644). Then, we reduced the data following the same procedure as our scientific data and performed aperture photometry on the calibration data using the *apphot* task in the NOAO/DIGIPHOT package in IRAF. From the measured count rates of the pre-SM3B data and the pre-SM3B photometric conversion factors (PHOTFNUs), we computed the flux of the standard star through each polarizer. Finally, we obtained the post-SM3B PHOTFNUs from the derived flux of the standard star and the measured count rates of the post-SM3B data. The measured count rates of the scientific data were then converted into Janskys. Table 2 summarizes PHOTFNU values we used.

Using the photometric calibrated data for each polarizer, we derived the Stokes parameters following the matrix inversion method Hines, Schmidt, & Schneider (2000); Dickinson et al. (2002). For the post-SM3B data, we used revised matrix coefficients provided by the STScI NICMOS group, of which only the t_k coefficients (which are related to the throughput of the polarizers) have been updated from the pre-SM3B values. The t_k values are listed in Table 2.

3.4. PSF Subtraction

To measure correct polarization strengths, the PSF effects have to be removed. Thus, we need to confirm the polarization free nature of our PSF standard star, HD 12088. Fig. 1 shows the I and I_p maps of HD 12088 and of an archived polarimetric standard star, BD+32°3739. HD 12088 does not appear to be extended (besides the more pronounced PSF spikes and polarizer ghosts) with respect to BD+32°3739 in I (Figs. 1a and 1b). The I_p map (Fig. 1c) does not seem to indicate the presence of intrinsic polarization from HD 12088 other than the known polarizer ghosts appearing at $(0''23, 1''19)$ and $(-0''16, 0''93)$ in comparison with BD+32°3739 (Fig. 1d). The excess I_p structure is likely due to photon shot noise

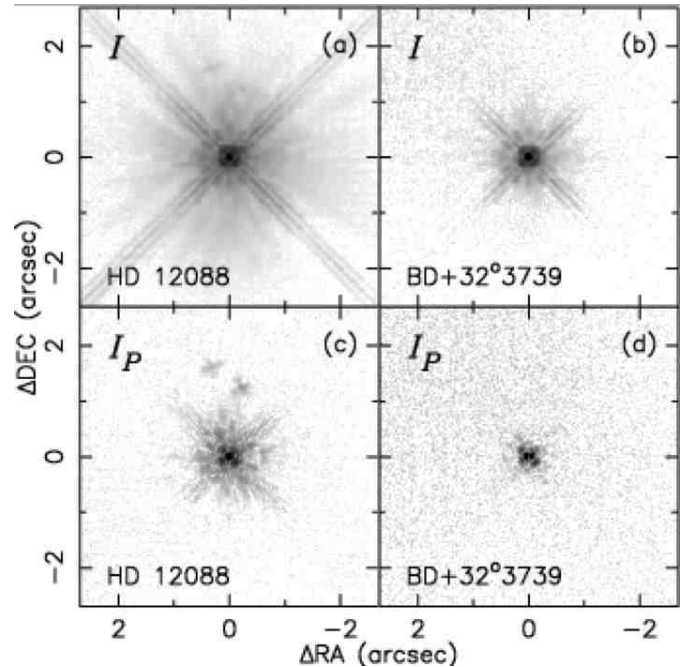


FIG. 1.— The I (top) and I_p (bottom) maps of our PSF standard, HD12088 (left), and an unpolarized standard, BD+32°3739 (right). The maps are centered at the position of the star and the tickmarks indicate the RA and DEC offsets in arcsec. The data +y direction points up and the data +x direction to the left: the PSF structure and polarizer ghost show at the same location.

caused by the bright star and is restricted mainly to $\lesssim 0''6$ from the star. The measured polarization is 1.5% in a $0''6$ diameter aperture (about $\times 3$ larger than the FWHM of the PSF) and 2.8% in pixels registering $> 10\sigma_{\text{sky}}$ in the I map for HD 12088, while that for BD+32°3739 is 1.8% and 1.4%, respectively. Hines, Schmidt, & Schneider (2000) reported $\lesssim 1\%$ instrumental polarization. Thus, our $\gtrsim 1\%$ polarization of BD+32°3739 is likely due to systematics in the data reduction procedure. Slightly higher polarization of HD 12088 in the $> 10\sigma_{\text{sky}}$ pixels is likely due to the polarizer ghosts and pixels affected by the PSF spikes. Therefore, we consider that polarization in HD 12088 is negligible for our purposes in detecting polarization much higher than a few % and that such small polarization would not affect our interpretation of the data.

Closer inspection of Figs. 1a and 1b indicates that there is a companion object very close to HD 12088 at $(-0''19, 0''09)$. Although such a companion can be removed by combining images rotated by a multiple of 90deg around the central star, it turned out that this operation would average out the asymmetric PSF structure to a degree that the PSF subtraction would not be effective. Thus, we performed PSF-subtraction simply using the raw HD 12088 maps: the resulting PSF-subtracted maps would suffer from oversubtraction by this companion object.

For the PSF removal, we tried deconvolution using the Lucy-Richardson method (the *lucy* task in IRAF) and the MCS method (Magain, Courbin, & Sohy 1998). However, deconvolution did not yield satisfactory results because (1) the PSF effects were too severe and extensive to be removed and (2) the companion objects interfered with the deconvolution algorithm. Thus, we resorted to a much simpler scale-and-shift subtraction approach. The intensity scaling factor and shifts between the images were found by iteratively search-

ing for the best values using the PSF spikes, since we did not know *a priori* how much intrinsic nebular flux there is in addition to the stellar flux and the pixels over the central star were often susceptible to large photon shot noise. It should be noted that the HD 12088 data are only effective for our target data obtained with NIC1 polarizers after SM3B. For PSF subtraction in pre-SM3B NIC2 data, we used the BD+32°3739 data.

Fig. 2 demonstrates improvements gained from PSF subtraction. The raw I map (Fig. 2a) is severely affected by the PSF, and it is nearly impossible to gain any spatial information about the nebulosity except that it is extended. However, the PSF-subtracted I map (Fig. 2b) successfully reveals the *internal* shell structure. The raw I_p map (Fig. 2c) shows even more shell structure than the PSF-subtracted I map: polarized light seems to be concentrated at the periphery of the nebulosity with local brightness enhancements. However, we now recognize the intrusive PSF spikes and polarizer ghosts at $(-0''.8, -0''.9)$ and $(-1''.4, -0''.8)$ due to photon shot noise caused by the extremely bright central star (Fig. 2d) shows the PSF-subtracted I_p map in which the shell structure is seen almost artifact-free. However, the quality of the image is gravely compromised by the S/N of the PSF standard data. This is why data from the polarimetric standard star have to be carefully tailored in imaging polarimetry for optically thin circumstellar shells surrounding a bright central source. Unfortunately, we did not have an independent orbit for PSF observations. Hence, our PSF data was unable to gain enough S/N to achieve optimum results from PSF subtraction. In the following, we use raw I_p data in order to take advantage of high S/N unless the polarizer ghosts pose serious problems in the data analysis. As for the P maps, we use raw P data for displaying purposes, but measurements were done with the PSF-corrected data.

4. RESULTS

In Figs. 3 to 7, we present the polarimetric maps of five PPNs in a uniform format. The PSF-subtracted I and I_p (top left and right, respectively) maps reveals the distribution of scattering medium in these circumstellar shells. The P map (bottom left) represents the distribution of I_p with respect to I , augmenting the I and I_p maps from a different point of view. The θ map shows the orientation of the polarization vectors by the “rainbow wheel” pattern. We opt to display the θ maps this way since the high resolution quality of the data can be compromised by inevitable rebinning in making conventional vector diagrams. In addition, the pixels affected by image anomaly (by the ghosts and shot noise near the central star) have been masked out in the θ maps.

In Table 3 we summarize the results of the observations including the measured coordinates of the object, I and I_p fluxes, mean P and its standard deviation, and descriptions of I_p structure. The coordinates listed are the observed location of the I peak, which coincides with the I_p peak and the θ center if the shell is sufficiently optically thin. The fluxes are determined by integrating the surface brightness over the shell where pixels register more than one σ_{sky} . Although sky emission has been subtracted in calibration, we removed any residual “sky” emission if the sky value determined in an annulus around the object registers more than three σ_{sky} . The mean P and its standard deviation have been determined by using pixels that registered more than 10 σ_{sky} . The I_p structure is described by the overall shape, dimensions (typically major and minor axis lengths), and PA measured east of north.

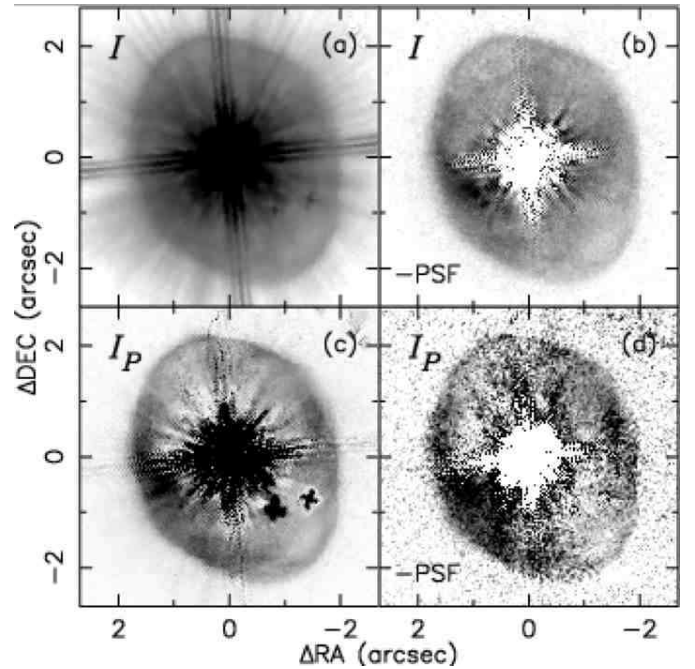


FIG. 2.— The I (top) and I_p (bottom) maps of IRAS 07134 derived from the raw (left) and PSF-subtracted (right) data. The maps are in the standard orientation (N is up, E to the left) and centered at the central star with tickmarks showing the RA and DEC offsets in arcsec. Detailed shell structure can be seen in the PSF-subtracted I map, and even better in the I_p maps. While the PSF-subtracted I_p map shows almost artifact-free structure of the shell, it is degraded from the low S/N of the PSF standard data.

The accuracy of the photometric results depends on the quality of the PHOTFNU values used in our analysis (Table 2). The measured I fluxes are all consistent with the known photometric values, given the difference in the filter profiles between J/K and short/long wavelength polarizers, except for IRAS 07134. Our IRAS 07134 observations have yielded the I flux of 9.3 Jy, which is more than a factor of three higher than recent measurements of 2.9 Jy ($m_J = 6.8$; e.g. Ueta et al. 2003). While this source suffers from the polarizer ghosts, they are known to cause only less than 1% in brightness of the primary source (Hines, Schmidt, & Schneider 2000). Thus, the ghosts alone could not have introduced this inconsistency. Given that our PHOTFNU have yielded reasonably consistent photometric results for the other three targets (within 50% difference), our estimates of the PHOTFNU values do not seem to have caused systematic errors. The most likely source of this inconsistency seems to be the photon persistence. The data for IRAS 07134 are affected by severe photon persistence, and the affected pixels ($\sim 0''.4$ of the star) can remain affected even two dither positions later (i.e., four exposures or more later). The persistent signal decay can interfere with the non-linearity correction algorithm in the pipeline calibration, leading to inaccurate count rates. We have not, however, attempted to improve the accuracy of our photometric measurements, since (1) absolute photometric calibration is not possible without properly calibrated PHOTFNU values, (2) only relative calibration among the three polarizers is important in deriving the Stokes parameters (Q and U), and (3) only the vicinity of the star ($\sim 0''.4$) is affected by the photon persistence.

With the (P, θ) data set, we see highly centrosymmetric nature of polarization in all PPNs. We can use the polarization

TABLE 3
SUMMARY OF *HST*/NICMOS POLARIMETRIC RESULTS

Source	Measured Coord. (J2000) ^a		Band ^b	Flux		$\langle P \rangle^c$ (%)	I_p Structure		
	RA	DEC		I (mJy)	I_p (mJy)		Morphology	Size (")	P.A. (°) ^d
IRAS 07134	07 16 10.27	+09 59 48.5	POL-S	9300 ^e	2000 ^e	55 ± 16	Elliptical/Round Hollow Shell	4.8 × 4.0	25
IRAS 06530	06 55 31.80	-02 17 28.3	POL-S	380	67	47 ± 15	Elliptical Shell + Bipolar Cusp	2.7 × 1.0	20
IRAS 04296	04 32 56.95	+34 36 13.1	POL-S	340	60	40 ± 12	Quadrupolar		
							Elliptical (extension 1)	2.1 × 0.7	26
							Elliptical (extension 2)	3.5 × 0.5	99
IRAS 02229	02 26 41.79	+62 21 22.2	POL-S	4800	1200	52 ± 19	Elliptical	2.1 × 1.3	59
IRAS 16594	17 03 10.04	-47 00 27.0	POL-L	620	66	39 ± 16	Elliptical + Protrusions	5.0 × 2.2	104

^aOf the I peak location.

^bPOL-S: 0.8–1.3 μ m, centered at 1.1 μ m; POL-L: 1.89–2.1 μ m, centered at 2.05 μ m

^cMean P and its standard deviation.

^dDegrees E of N.

^eThe measured I flux value is three times higher than the previously observed value; this is in part due to photon persistence. See text for details (§4).

TABLE 4
OFFSETS BETWEEN THE
ILLUMINATION SOURCE
AND THE I PEAK

Source	Offsets (arcsec)
IRAS 07134	0.08 ± 0.27
IRAS 06530	0.04 ± 0.20
IRAS 04296	0.06 ± 0.17
IRAS 02229	0.12 ± 0.31
IRAS 16594	0.06 ± 0.14

vectors to backtrack the position of the illumination source, i.e., the central star. The center of the vector pattern was derived by minimizing the sum of the square of the distance between the vector position and the vector pattern center. In this analysis, we used vectors that are in the pre-defined annulus centered at the presumed pattern center. We assumed the I peak to be the pattern center, and iterated the process by using the updated center position until the shift between the previous and current centers becomes smaller than the numerical accuracy of the analysis. The vector pattern center was found to coincide with the I peak position in all cases: the results are summarized in Table 4. Thus, these nebulae - SOLE-toroidal PPNs - are indeed optically thin and illuminated by the central star located at where the I peak is.

5. INDIVIDUAL SOURCES

In this section, we describe the individual source structure, including the 3-D aspects of it as revealed by these polarimetric images.

5.1. IRAS 07134+1005 (HD 56126)

Polarization observations of IRAS 07134 (HD 56126) are presented in Fig. 3. The PSF-subtracted I map (Fig. 3a) shows a slightly elliptical nebula (4.''8 × 4.''0 at PA 25°), which clearly possesses some internal structure previously unrecognized in the near-IR. The bulk of surface brightness is concentrated in the region close to the minor axis of the nebula (PA 115°), with the eastern side being brighter and spatially more extended than the western side. There is an apparent brightness peak on the east side of the nebula at (1'', -0.''5), whereas the west side does not show any local brightness peak. At

the northern and southern end of the nebula, there is significantly less surface brightness. There appears to be a filamentary structure along the periphery of the nebula, delineating the elliptical tips in the low surface brightness region (also seen well in the grayscale image, Fig. 2b).

In the I_p map (Fig. 3b), we can identify at least two regions of enhanced surface brightness on the east and west side of the nebula with the local peaks located at (1'', -0.''5) and (-1.''5, 0.''5). The east peak shows stronger and more extended brightness distribution than the west peak. The surface brightness of the east peak is 18 mJy arcsec⁻² which is about 1.5 times brighter than the western counterpart (see the profiles in Fig. 9). The region of enhanced surface brightness ($\gtrsim 5$ mJy arcsec⁻²) extends from PA 50° to 205° on the eastern side, and from 250° to 350° (with an apparent gap at 320°) on the western side. These brightness-enhanced regions are connected by the lower brightness (~ 3 mJy arcsec⁻²) region at the N-S elliptical tips of the nebula, in which filamentary structures outline the edge of the tips (more apparently in I_p than in I). Incidentally, the interior region encircled by this “rim” region shows weak surface brightness ($\lesssim 3$ mJy arcsec⁻², in the region $\lesssim 1.''2$ – $1.''3$ from the center). Overall, the bulk of I_p appears radially confined to the nebula periphery beyond about 1.''5 from the central star in all directions. This is particularly seen well in the northern half of the nebula where surface brightness of the interior region ($\lesssim 1.''5$ from the central star) becomes very small (almost null) without any contamination by the polarizer ghosts

In the P map (Fig. 3c), we immediately see that the high P ($\gtrsim 20\%$) regions occur near the periphery of the nebula beyond about 1.''5 from the central star in all directions: the mean polarization strength is 55%. The high P regions correspond to the high I_p regions. However, in the P map, there is not so much of a difference in the polarization strength at the elliptical tips and at the eastern/western edges of the nebula as in the I_p map. The northern tip shows somewhat weaker polarization strengths than the southern tip: this is consistent with slightly higher I in the northern tip and almost equal I_p at the both tips. The θ map (Fig. 3d) illustrates the polarization PA by the image tone. This particular θ map shows an almost perfect “rainbow wheel” pattern by the uniform and symmetric gradation of the image tone in the azimuthal direction, which depicts the highly centrosymmetric nature of the polarization.

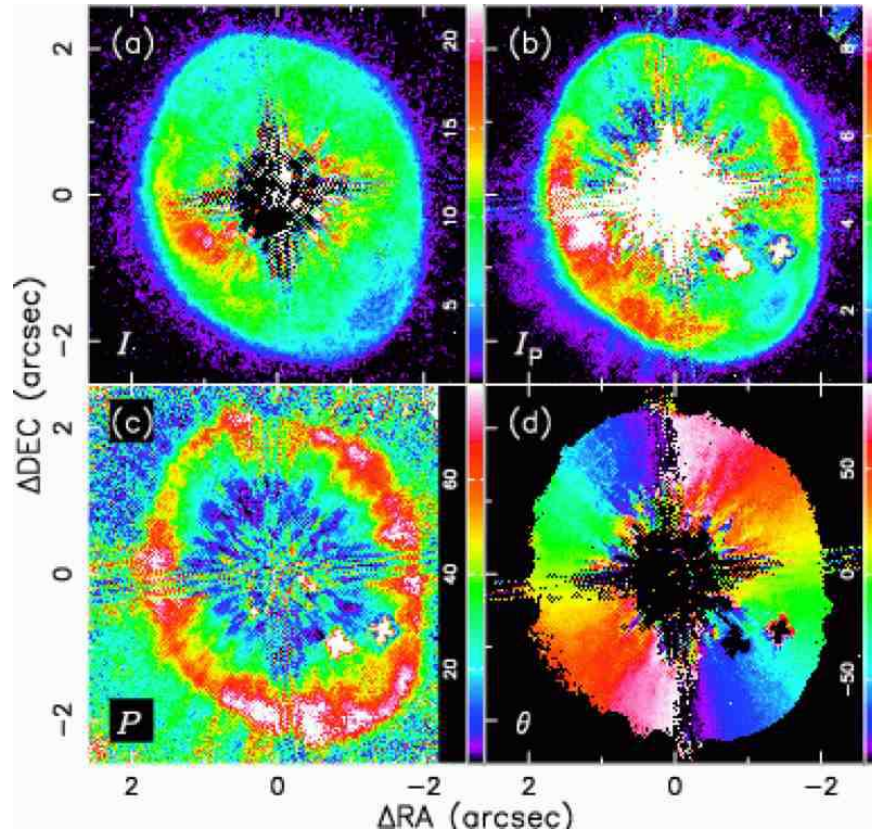


FIG. 3.— Polarimetric maps of *IRAS 07134+1005*: (a) the total intensity (I), (b) polarized intensity (I_p), (c) polarization strengths (P), and (d) polarization PA (θ), respectively from left to right, top to bottom. The maps are in the standard orientation (N is up, E to the left) and centered at the θ center with tickmarks showing the RA and DEC offsets in arcsec. The wedges indicate the scale of the image tone: mJy arcsec^{-2} in I and I_p , percentage in P , and degrees east of north in θ (i.e. PA 0° means the polarization vector, which is perpendicular to the scattering plane, is oriented in the N-S direction). In displaying the θ map we used pixels which register S/N of $> 10 \sigma_{\text{sky}}$ in the I map.

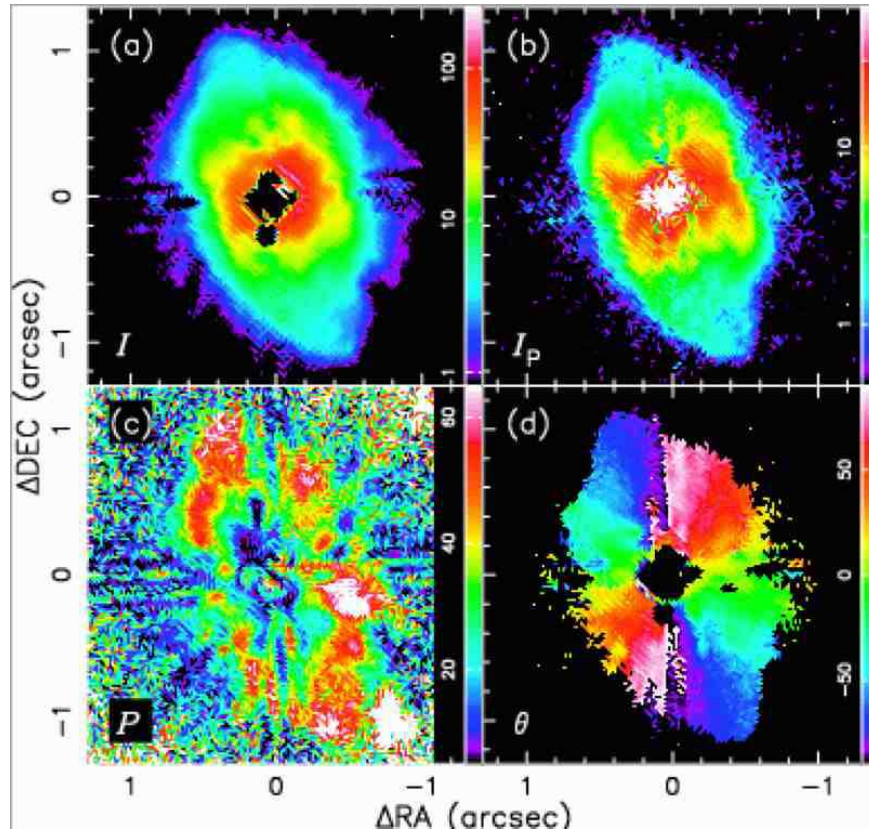


FIG. 4.— Polarimetric maps of *IRAS 06530-0213*. The display convention is the same as Fig. 3.

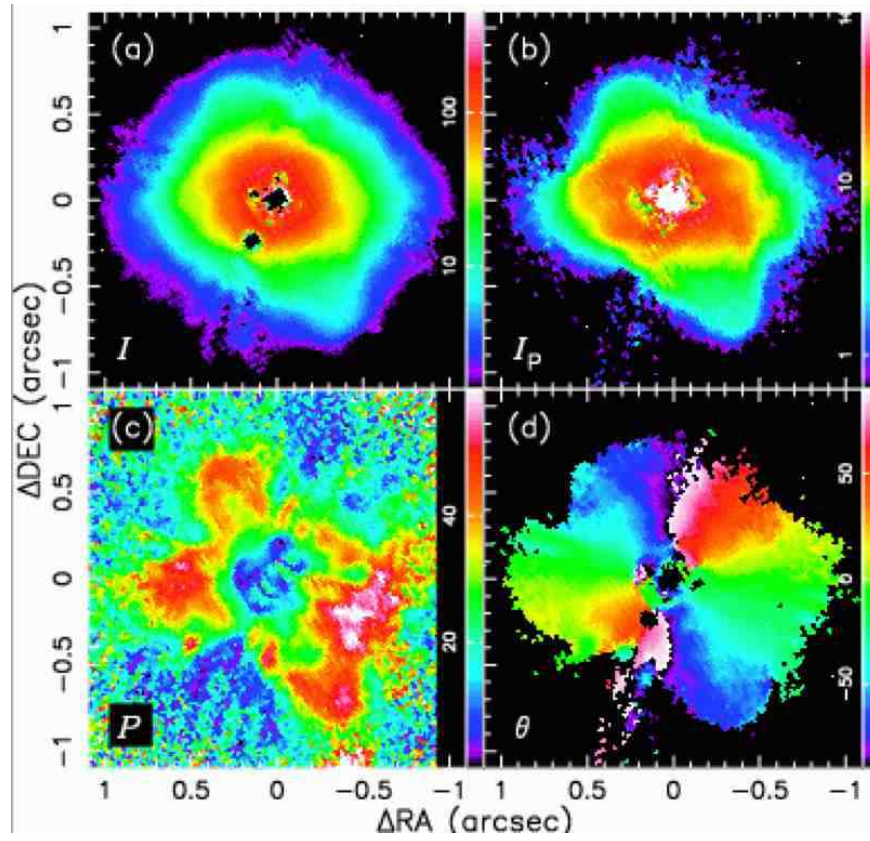


FIG. 5.— Polarimetric maps of *IRAS* 04296+3429. The display convention is the same as Fig. 3.

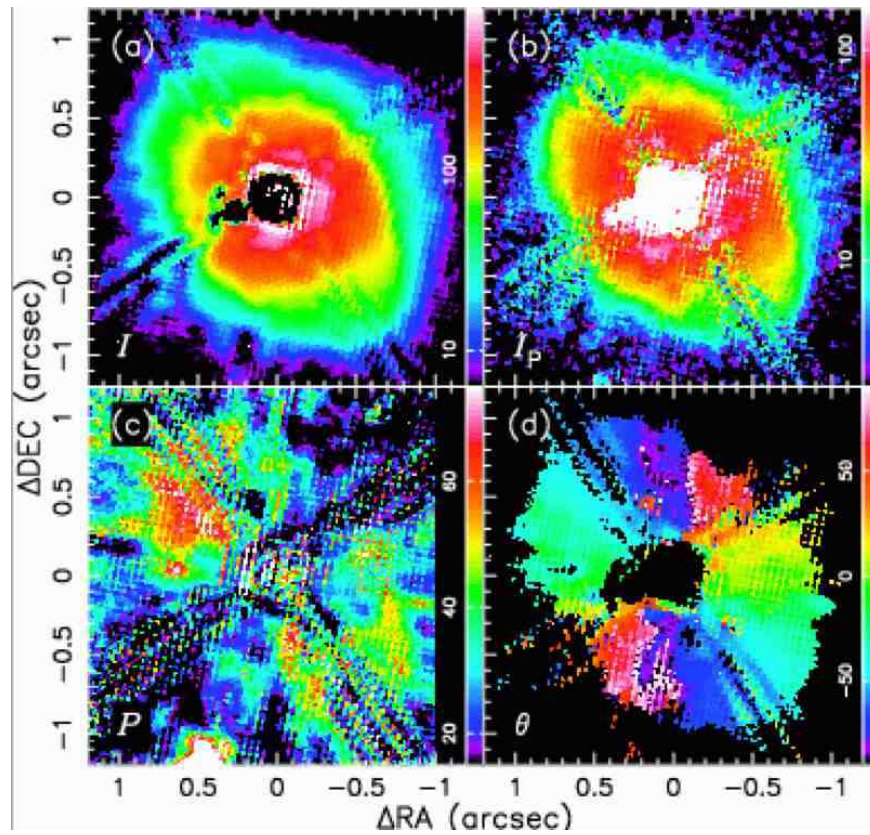


FIG. 6.— Polarimetric maps of *IRAS* (z)02229+6208. The display convention is the same as Fig. 3.

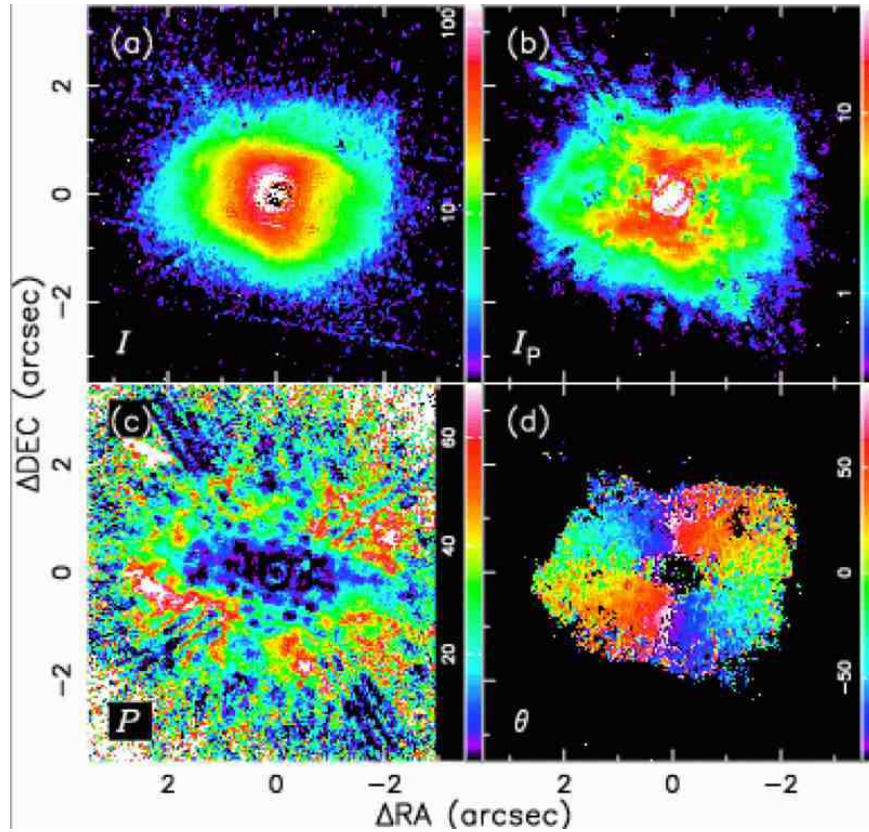


FIG. 7.— Polarimetric maps of *IRAS* 16594–4656. The display convention is the same as Fig. 3.

The past observations of this PPN found a slightly elliptical nebula via dust-scattered star light in the optical (Ueta, Meixner, & Bobrowsky 2000) and its two-peaked core structure via thermal dust emission in the mid-IR (Meixner et al. 1997; Dayal et al. 1998; Jura, Chen, & Werner 2000; Kwok, Volk, & Hrivnak 2002). The observed morphology has been thought to represent an almost edge-on ellipsoidal (slightly prolate) shell with an equatorial density enhancement (i.e., torus) that results in limb-brightened two-peak core emission in the mid-IR. This interpretation has been corroborated by a 2-D radiative transfer model of dust emission (Meixner et al. 1997, 2004). The present observations have revealed the toroidal structure of the shell for the first time in dust-scattered star light in the near-IR at more than a factor of two better resolution than the past mid-IR imaging. Moreover, the polarization characteristics of the shell confirm that it is optically thin at $1 \mu\text{m}$ having the central star as the illumination source. This further strengthens the edge-on torus interpretation, in which such density structure would manifest itself as two limb-brightened peaks only when the shell is sufficiently optically thin.

In Fig. 8, we compare the shell structure seen in dust-scattered near-IR light (color) and in thermal dust emission at $10.3 \mu\text{m}$ (contours; from Kwok, Volk, & Hrivnak 2002). Both data show similar brightness distribution where the eastern side is stronger and covers a larger spatial extent: even the surface brightness gap on the western side at PA 320° is seen in both of the I_p and $10.3 \mu\text{m}$ maps. Thus, we confirm that the imbalance of brightness distribution is real, and so is the isolated emission blob north of the central star seen in

the mid-IR. Geometrically, this blob appears to be part of the western edge of the toroidal structure that has been broken off for some reason.

There has been a question of whether this imbalance of mid-IR peak strengths is due to density or temperature effects of dust grains. If the dust temperature were the cause for the peak strength imbalance, we would not have seen the same imbalance in the I_p map. Polarization maps are sensitive to scattered light, whereas thermal dust emission maps are sensitive to warm dust. Thus, the I_p distribution does not necessarily have to follow the distribution of thermal mid-IR emission. Together with the mid-IR data, our images suggest that there is simply more dust grains in the eastern side of the shell than the western side. Recent CO observations have shown a similar morphology (Meixner et al. 2004), corroborating that there is more matter (dust and gas alike) on the eastern side of the shell in this object.

Meanwhile, there are apparent differences between the I_p and mid-IR morphologies which can be easily understood by the differences in the nature of light arising from dust grains. One difference is that the I_p and mid-IR peaks do not spatially coincide: the I_p peaks are found more towards the edge of the shell than the mid-IR peaks. In general, mid-IR emission arises from the warmest (~ 100 to 200 K) dust grains located near the inner edge of the shell. Thus, we would expect the mid-IR peak at the edge of the inner cavity where the line of sight traverses the longest distance in the warmest dust. However, due to the curvature of the surface of the inner cavity, the peak mid-IR position tends to be found somewhat closer to the central star. On the other hand, I_p becomes the strongest at the inner boundary and decreases in the radially outward

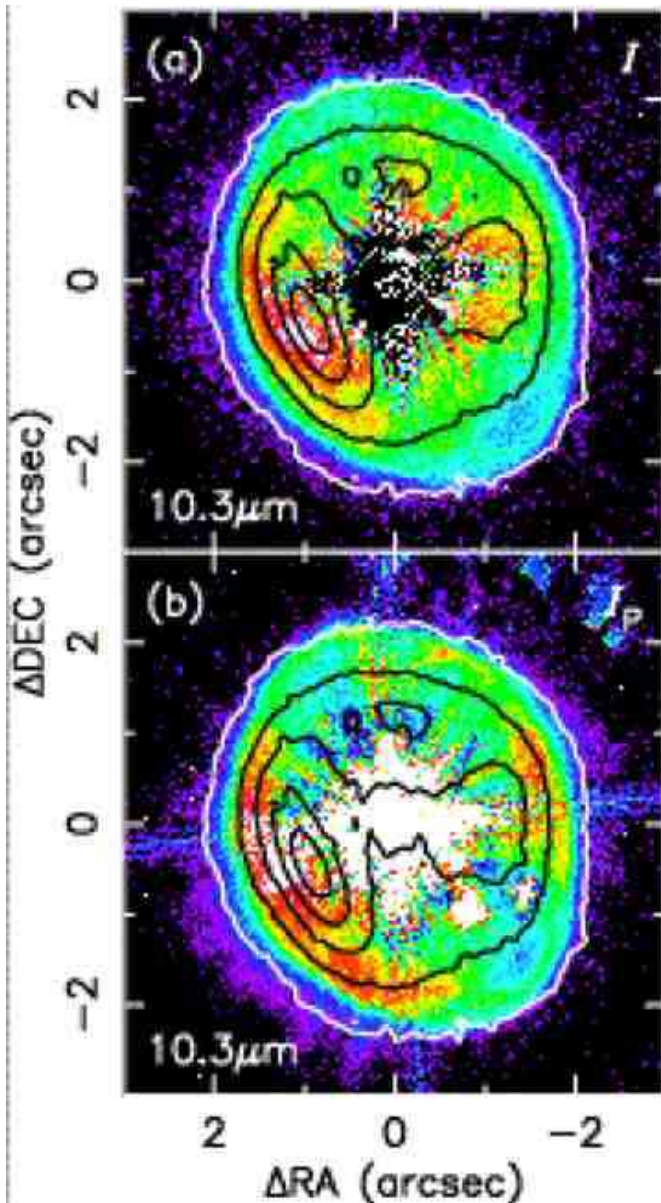


FIG. 8.— Spatial relationship between dust-scattered light (I [top] and I_p [bottom] maps in color) and thermal dust emission ($10.3\ \mu\text{m}$ contours at 10, 30, 50, 70, and 90%; Kwok, Volk, & Hrivnak 2002). The display convention is the same as Fig. 3.

direction assuming a radially decreasing density profile (e.g. $\propto r^{-2}$), because scattering geometry dictates the behavior of scattered light. Another difference is that the I_p peaks are more extended along the nebula edge than the mid-IR peaks. This is simply because scattering can occur as long as there is enough incident light and scattering medium. Thus, the I_p map has unveiled the shell structure in the outer shell where the region of enhanced density is extended well into the high latitude part of the ellipsoidal shell.

As a PPN, *IRAS 07134* is expected to have an inner cavity generated by the cessation of mass loss at the end of the AGB phase. The emission structure of the mid-IR and CO maps (e.g. Kwok, Volk, & Hrivnak 2002; Meixner et al. 2004) is consistent with the presence of such a cavity. If the shell of *IRAS 07134* is hollow and has a radially decreasing density structure, then we expect that (1) the highest I_p occurs at the

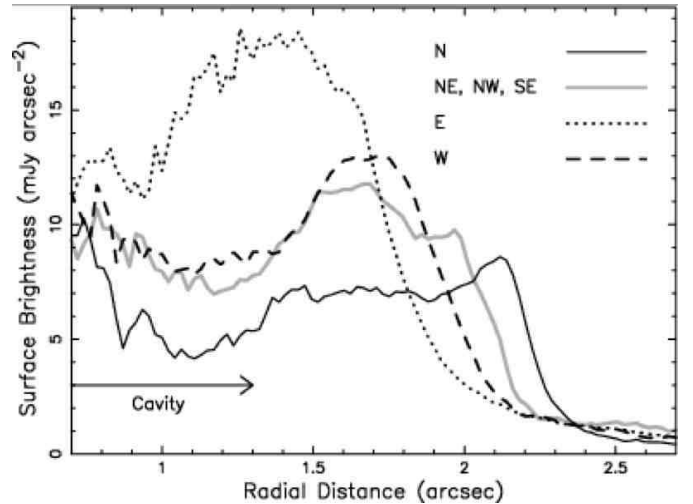


FIG. 9.— Polarized brightness profiles of *IRAS 07134*: N cut (at PA 25° ; black solid line), NW-NW-SE cut (average of cuts at intermediate PAs 70° , 160° , and 340° ; gray solid line), E cut (at PA 115° ; dotted line), and W cut (at PA 295° ; dashed line).

inner edge of the shell and (2) P should radially increase due to the geometrical effect of scattering angles (confined closer to 90°) and becomes the highest at the outer edge of the shell. Our I_p and P maps do show these characteristics exactly as expected. Although it is still possible that the contamination by the unpolarized component of the PSF artificially lower P in the central region, the high P ($\gtrsim 20\%$) region is restricted near the outer edge of the shell beyond the PSF. This high P regions occupy the same portions of the shell as the high I_p regions, forming a “ring” structure at the rim of the shell. Therefore, the shell of *IRAS 07134* most likely possesses an inner cavity, and the part of the shell probed by scattered light represents a hollow spheroid.

To better illustrate the spatial variation of surface brightness, we have made various cuts in the I_p map. In Fig. 9, we show profiles along the northern major axis (N cut; PA 25° ; solid black line), eastern minor axis (E cut; PA 115° ; dotted line), western minor axis (W cut; PA 295° ; dashed line), and intermediate PAs (NE-NW-SE cut; PAs 70° , 160° , and 340° ; solid gray line). These profiles are derived from a linear cut of 10-pixel width (or the median of multiple cuts, in the case of the NE-NW-SE cut). We do not include the S and SW cuts because of the contamination by the polarizer ghosts.

These cuts show a similar profile: there is a steep outer edge representing dust pile-up, which surrounds the high brightness region of the main shell, and the brightness steeply falls down to a relatively flat, plateau region. All cuts show the inner plateau inward of $\lesssim 1''.3 - 1''.4$, except for the E cut with plateau of $\lesssim 0''.9$. We interpret that this inner “plateau” profile is due to the inner cavity created by a precipitous drop in the mass loss rate at the end of the AGB phase. In the context of polarization, the presence of the inner cavity means the absence of the scattering medium near the plane of the sky, resulting in an abrupt decrease of I_p and P , thereby forming an inner boundary of the shell. It is, therefore, the direct observational evidence for the presence of such an inner cavity in PPNs.

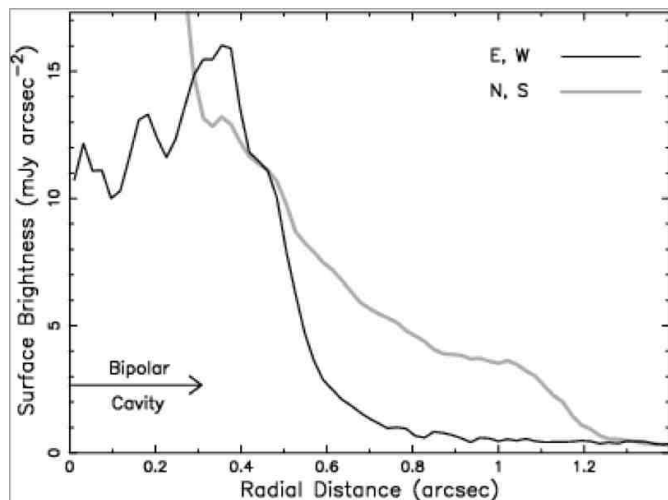


FIG. 10.— Polarized brightness cuts of *IRAS* 06530: N-S cut (average of N and S profiles at PA 20° and 110° ; gray solid line) and E-W cut (average of cuts along lines perpendicular to the major axis $0''.43$ N and S of the equatorial plane; black solid line).

The polarization maps of *IRAS* 06530 are displayed in Fig. 4. The PSF-subtracted I map (Fig. 4a) shows a highly elliptical shape of the nebula ($2''.4 \times 1''.1$ at PA 20°), in which the low brightness (~ 5 mJy arcsec $^{-2}$) elliptical tips extend beyond the barrel-shaped region of higher surface brightness ($\gtrsim 15$ mJy arcsec $^{-2}$). The I_p map (Fig. 4b) reveals a cusp-like (or a sideways x) structure within the barrel region. Such structure typically indicates the swept-up walls of the bipolar cavities. Thus, *IRAS* 06530 is likely a near edge-on, highly prolate ellipsoidal shell showing a rather bipolar nature in the low latitudinal region. Fig. 10 shows the polarized brightness cuts of the shell made along the major axis (N-S cut; N-S averaged, thick gray line) and the lines parallel to the minor axis at $0''.43$ N and S of the central star (E-W cut; E-W averaged, solid black line). The N-S cut demonstrates the elongated I_p structure with a gentle slope at the edge, while the E-W cut shows a peak at around $0''.34$ that defines a bipolar cavity wall. The polarization characteristics seen in the P and θ maps (Fig. 4c and 4d, respectively) are very similar to those of *IRAS* 07134 (Fig. 3). P is stronger near the edge of the shell while it is absent in the central region even beyond the PSF. The polarization pattern is very much centrosymmetric as seen from the almost perfect rainbow wheel pattern.

Thus, *IRAS* 06530 is a highly prolate spheroidal shell, which very likely has an inner cavity as in *IRAS* 07134. Although the shell is optically thin, there is sufficiently high concentration of dust grains at the equatorial region so that the bipolar cusp structure is seen in I_p . The total optical depth is not large enough to induce the full extinction of star light expected in typical bipolar PPNs (e.g., *IRAS* 17150–3224; Kwok, Su, & Hrivnak 1998; Su et al. 2003). This may be why we do not observe a low I_p “hole” in the central region of the shell as we saw in *IRAS* 07134. However, we do see a possible inner cavity in the P map.

5.3. *IRAS* 04296+3429

In Fig. 5 we present data from *IRAS* 04296. The PSF-subtracted I map (Fig. 5a) shows a quadrupolar nebula (roughly $1'' \times 1''.5$) with an east-west elongated core having round protrusions towards PA 26° and 206° . The I_p map (Fig. 5b) successfully unveils the slanted X shape of the nebula

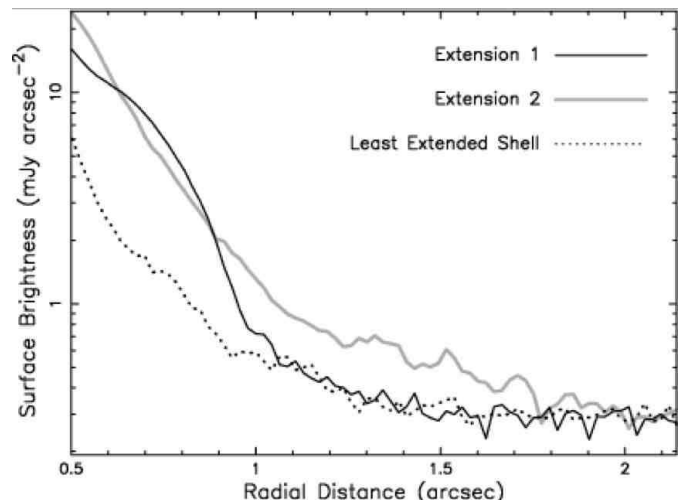


FIG. 11.— Surface brightness radial profiles of *IRAS* 04296: of the extension 1 (at PA 26° ; black solid line), of the extension 2 (at PA 99° ; gray solid line), and of the least extended part of the shell (the average of the cuts at PA 63° and 153° ; dotted line).

more clearly than the I map. The nebula’s X shape is due to the presence of two axes of elongation. One of the elongations is oriented at PA 26° and shows a relatively well-defined elliptical shape ($2''.1 \times 0''.7$; extension 1). The other elongation, oriented at PA 99° , is fainter with its surface-brightness-limited ends smeared out in the background ($3''.5 \times 0''.5$; extension 2). These elongations are not oriented perpendicular to each other. Although Sahai (1999) reported that extension 2 is not straight with a 5° shift between the eastern and western tips from the WFPC2 data, we are unable to confirm this in our data due to the confusion by the PSF spike nearly aligned with this extension. While the I_p structure is consistent with the one seen in the previous WFPC2 data (Ueta, Meixner, & Bobrowsky 2000) the central star appears more prominently in the near-IR data, since the central star (the nebula) is brighter (fainter) in the near-IR. This is why the I map does not clearly show the X structure as in the WFPC2 images.

Fig. 11 displays I_p radial profiles of the extensions to better present the extent of the structures. These profiles are constructed by taking linear cuts of 10-pixel width along the extensions and averaging the values at both ends. For comparison, we also show the “least extended” shell profile, created from linear cuts at PA 63° and 153° (in-between directions of the extensions). The extension 1 profile (black solid line) shows I_p excess in the region close to the central star, but it suddenly falls to the flux level similar to the least extended profile (black dotted line) at around $1''$. On the other hand, the extension 2 profile exhibits I_p excess as far out as $\sim 1''.8$ before it gradually falls down to the background level.

The P map (Fig. 5c) uncovers the structure of the two extensions even better. In extension 1, strongly polarized light ($\gtrsim 30\%$) is concentrated near the periphery of the elongation, especially at the tips, whereas weakly polarized light fills the cavity surrounded by the high polarization region. Because of the compactness of the nebula, we can not rule out the possibility that the central region registers low P values due to the residual unpolarized component from the central star. The P structure of extension 1 resembles that of the previous two sources. However, in extension 2, the weak P cavity is not very well-defined partly due to confusion by the presence of

falsely high polarization caused by the PSF spikes. Nevertheless, high polarization is observed as far out as $1''$ from the central star. The θ map (Fig. 5d) exhibits a general centrosymmetric pattern of an optically thin shell, with only a marginally shallower gradient over the extensions.

Based on the optical morphology of the nebula, Sahai (1999) interpreted extension 1 to be a bounded disk that collimated outflows manifesting themselves as extension 2. Our polarization data, however, do not support this disk interpretation. The I_p shape of extension 1 does not support a geometrically thin disk structure. If extension 1 is a thin disk with its plane inclined 24° with respect to the line of sight, the spatial distribution of the disk material in the plane of the sky will be extremely restricted. This would result in strong scattering in a geometrically narrow region in the sky, and the I_p map will likely be very narrow in the direction perpendicular to the extension. However, this is not the case. The fact that extension 1 appears elliptical in I_p strongly suggests that the distribution of scattering matter is elliptical in the plane of the sky, implying a prolate spheroidal structure of the shell. The P morphology of extension 1 shows a possible low P cavity surrounded by the region of strong polarization at the nebula edge. Thus, extension 1 is very likely a prolate spheroid, possibly with an inner cavity. In terms of polarization characteristics, there is no significant difference in both extensions except for the sharpness of the tip structure. In extension 1, we see the highest P at the tips of the elongation. However, in extension 2, the highest P does not arise from the tips. As the profiles indicate in Fig. 11, extension 2 is extended out to about $1''.8$. This may suggest that extension 2 is also a hollow prolate spheroid, but is inclined with respect to the plane of the sky so that the region of high P occurs where the spheroidal shell intersects with the plane of sky and not at the tips.

5.4. IRAS (Z)02229+6208

We show the polarization maps of IRAS 02229 in Fig. 6. The PSF-subtracted I map (Fig. 6a) shows an elliptically extended nebula ($2''.1 \times 1''.3$ at PA 45°), which is consistent with the previous WFPC2 images (Ueta, Meixner, & Bobrowsky 2000). The surface brightness distribution is such that the southwestern tip is slightly brighter than the northeastern tip. The I_p map (Fig. 6b) exhibits the same elliptical shape of the nebula. Unlike the I map, the I_p map does not show any apparent spatial difference in the polarized surface brightness distribution. Although the low brightness edge (~ 50 mJy arcsec $^{-2}$) is elongated towards PA 45° (nearly aligned with a PSF spike), the high surface brightness core (> 200 mJy arcsec $^{-2}$) appears to be elongated towards a slightly different direction (PA 60°).

The P map (Fig. 6c) appears quite differently with respect to other P maps: strong polarization is not concentrated near the periphery in this nebula. Instead, we see a band of low polarization ($\lesssim 30\%$) in the middle of the shell aligned with PA 150° , which separates the region of medium polarization ($\sim 30\text{--}40\%$) on the southwest side and the region of high polarization ($\gtrsim 40\%$) on the northeast side. The θ map (Fig. 6d) shows a generally centrosymmetric pattern. However, the gradient of the vector angle seems to be steep in the low polarization band, and shallow in the elliptical tips of the shell. This indicates that more vectors in the elliptical tips are aligned parallel to the low P band which most likely represents the equatorial plane. Note also that the orientation of the low polarization band is not perpendicular to the direction of the elongation of the shell, but to that of the core elongation (PA

60°). The polarization characteristics of this object is very distinct with respect to those of the previous objects.

The peculiar P map can be understood in terms of the inner structure and inclination of the shell. The presence of the low P band suggests that dust density is more equatorially enhanced within a rather geometrically narrow region in this object. If the near side of this inner torus is tilted towards the northeastern direction, the southwestern side of the shell (i.e., the near side of the ellipsoidal shell) appears more illuminated by the direct star light in our viewing angle. This is consistent with the I map showing the brighter southwestern tip than the northeastern tip (Fig. 6a). However, assuming a spheroidal density distribution of the shell there will be no difference in terms of the amount of scattering medium in the plane of the sky, and hence, the I_p brightness will be the same on both sides of the shell (Fig. 6b). Since P is a ratio of I_p to I , we would see lower (higher) P on the southwestern (northeastern) side of the shell. Therefore, IRAS 02229 seems to be similar to IRAS 06530 with a spheroidal shell with a relatively stronger equatorial density enhancement. However, the shell orientation of IRAS 02229 is most likely more pole-on compared to IRAS 06530.

IRAS 02229 was marginally resolved in the mid-IR in our previous imaging survey (Meixner et al. 1999), and has recently been observed at the Gemini North (Kwok, Volk, & Hrivnak 2002). Fig. 12 shows the I_p and P maps overlaid with 10.3 and 18.0 μm contours. 10.3 μm emission is extended with PA of 20° , which is off by 25° with respect to the I elongation (Fig. 12a). We have also seen a slight shift of PA between the outer and inner I structure (45° and 60° , respectively). Assuming these parts of the shell with different PAs represent distinct portions of the shell structure, this shift of PA may indicate that the inner torus is precessing/rotating in the counterclockwise direction. Such precession/rotation of the inner torus has already been suspected in a SOLE-toroidal PPN, HD 161796 (Gledhill & Yates 2003).

The low P band also does not seem to show strong spatial correlation to the 10.3 μm emission region (Fig. 12b). However, the 18.0 μm map seems to be elongated in the direction of the low P band (Fig. 12c). Kwok, Volk, & Hrivnak (2002) suspected that the 18.0 μm map may have suffered from variable sky conditions. If IRAS 02229 has geometrically narrow density distribution in the innermost region of the shell, it is possible that the mid-IR continuum emission would be elongated along the equatorial plane as we see in Fig. 12c. If this geometry causes the 18.0 μm elongation, then this raises a question as to why the 10.3 μm emission, another map of continuum, is not elongated as the 18.0 μm map. The 10.3 μm map, in fact, is morphologically very similar to the 11.7 and 12.5 μm maps that represent unidentified IR feature emission. Although Kwok, Volk, & Hrivnak (2002) concluded that 10.3 μm emission represented continuum, comparison of the *ISO* spectrum with the mid-IR filter profiles (see Fig. 4 in Kwok, Volk, & Hrivnak 2002) may indicate that the 10.3 μm filter does capture some emission due to the same unidentified IR feature emission that caused elongation in the 11.7 and 12.5 μm images. It is also interesting to note that the 20.8 μm map (representing the unidentified “ 21 μm ” feature) shows somewhat different elongation with respect to other maps. Thus, it may be that the 18.0 μm map is the true continuum emission map that reflects the disk-like dust distribution of the shell, and that other maps are different due to distinct dust species responsible for feature emission at other wavelengths. Further investigation at higher resolution,

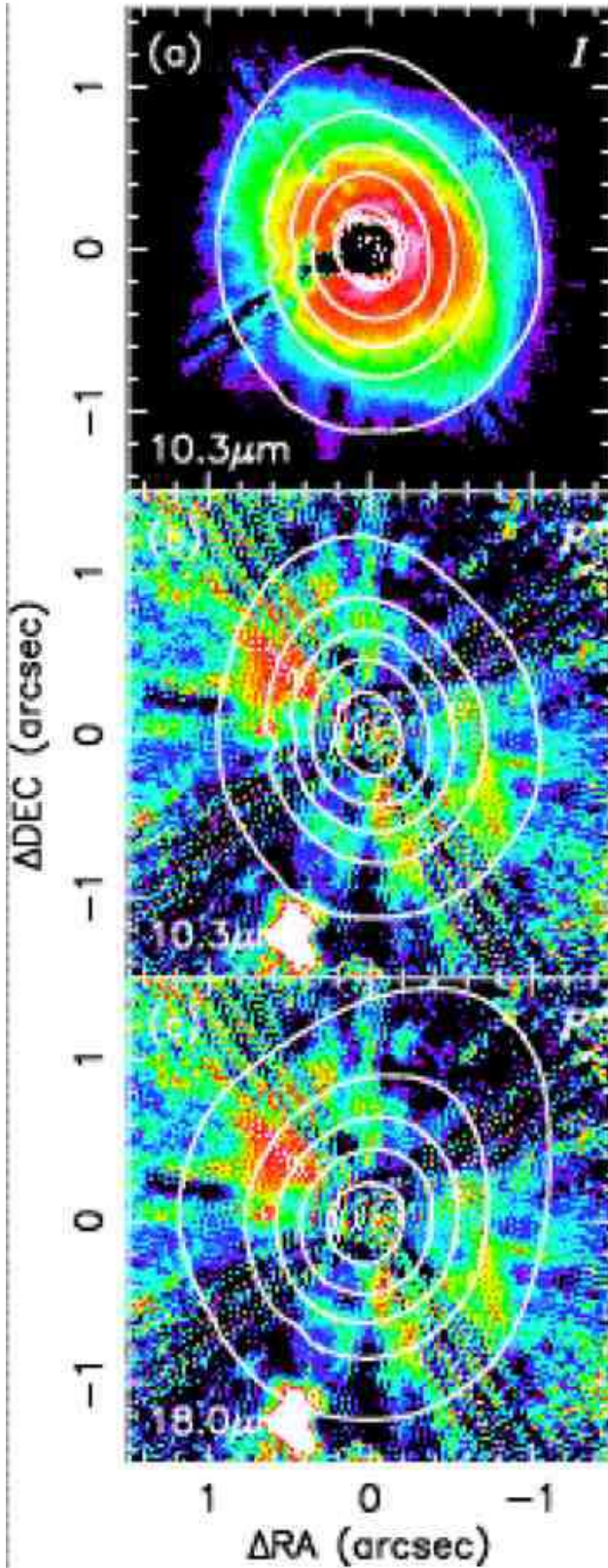


FIG. 12.— *IRAS 02229*: Spatial relationship between dust-scattered light and thermal dust emission (color I_p map and $10.3 \mu\text{m}$ contours; [a]), the polarization strength and thermal dust emission (color P map and 10.3 and $18.0 \mu\text{m}$ contours; [b] and [c], respectively). The mid-IR data are from Kwok, Volk, & Hrivnak (2002), and the contours are at 10, 30, 50, 70, and 90%. The display convention is the same as Fig. 3.

preferably spatial spectroscopy, is necessary to determine if distinct spatial distribution of different dust species can result in such changes of morphology.

5.5. *IRAS 16594–4656*

We present the archived $2 \mu\text{m}$ polarization data of *IRAS 16594–4656* that have been reanalyzed to mitigate the PSF effects (Fig. 7). The PSF-subtracted I map (Fig. 7a) reveals the inner structure of the nebula that is clearly elongated in the east-west direction ($5''.0 \times 2''.2$ at PA $81^\circ - 261^\circ$; $\gtrsim 7 \text{ mJy arcsec}^{-2}$). The I_p map (Fig. 7b) uncovers the structure of the shell, in which we see the bipolar cusp structure, similar to the one in *IRAS 06530* (Fig. 4b), corresponding to the main I elongation. We do not see any elliptically elongated tips surrounding the cusp structure as in the case for *IRAS 06530*. The tips of the cusp are more elongated in this object and appear to delineate the wall of the bipolar cavities.

The P structure resembles those with a hollow shell (Fig. 3c, 4c, and probably 5c), in which there is a region of low polarization in the middle of the shell encircled by a region of high polarization. In *IRAS 16594*, however, the region of high polarization does not seem to completely surround the central low P region: it is mainly found southeastern and northwestern ends of the shell. Moreover, it appears that the P map also possesses a low P band structure in PA 167° , which is similar to the one in *IRAS 02229* (Fig. 6c). The θ map is very much centrosymmetric.

IRAS 16594 has been observed with *HST* many times in the past. WFPC2 images have shown the object’s multipolar reflection nebula that has three extensions on each side (e.g., Hrivnak, Kwok, & Su 1999). These extensions form oppositely pointing pairs in the directions of PA $40^\circ - 220^\circ$, $60^\circ - 240^\circ$, and $80^\circ - 260^\circ$. The length of the elongation decreases in the counterclockwise direction, while the surface brightness increases. Thus, the optical structure has been interpreted as oppositely directed material ejected episodically from a rotating source. Our PSF-subtracted I and I_p images show that the inner shell structure is aligned with the elongation of PA $80^\circ - 260^\circ$, as has been seen only faintly in heavily PSF affected NICMOS broad to medium band images (Su et al. 2003). Hence, the episodic ejection interpretation is consistent with the nebula’s inner shell structure.

The toroidal nature of the innermost shell has recently been exposed by mid-IR imaging, in which the presence of the limb-brightened peaks in the emission core has proven that the shell has an equatorial density enhancement along PA 170° (García-Hernández et al. 2004). The elongation of the inner shell is therefore aligned with the symmetric axis of the torus. Thus, it seems likely that material ejection is presently channeled into the directions of the inner shell elongation by the torus or by some collimation mechanism(s) that can generate such outflows and equatorial density enhancement.

The orientation of the torus is spatially coincident with the low P band seen in our data (Fig. 7c). This confirms our interpretation of the presence of low P band as a manifestation of dust density enhancement along the equatorial plane of the system (see Fig. 6c and discussion associated with it). Su et al. (2003) interpreted that the low P around the central star was due to an inclined dust torus at an “intermediate” angle. However, the P map of *IRAS 16594* does not suggest an inclination angle as large as *IRAS 02229* in which the imbalance of I due to inclination resulted in the imbalance of P on the opposing sides of the shell. Thus, the orientation of the torus in *IRAS 16594* is more likely close to edge-on. A dust

emission model with our 2-D radiative transfer code has indicated the inclination angle of roughly 75° with respect to the line of sight (Ueta et al. 2004).

6. DISCUSSION

6.1. 3-D Shell Structure via (I_p , P)

Our main objective in the present study is to investigate the structure of *optically thin* PPNs by means of imaging polarimetry. We have made use of the (I_p , P) data set to achieve our goal instead of the more conventional (P , θ) data set with which *optically thick* regions of the circumstellar shells are probed through the way polarization vectors are aligned with respect to the equatorial plane (e.g. Whitney & Hartmann 1993; Su et al. 2003).

In radially decreasing density distribution typical of PPNs, I_p radially decreases. So, I_p becomes the strongest at the inner edge of the shell if the shell has an inner cavity as in the case of PPNs. In the optically thin regime where single scattering dominates, P in general becomes the strongest at the outer edge of the shell because of the geometrical effect. With the (I_p , P) data set, we have successfully detected both inner and outer edges of the shell in *IRAS* 07134. The data have shown that the polarized surface brightness distribution encircles the inner cavity, forming a complete “ring”. In terms of scattering geometry, such brightness distribution indicates a hollow spheroid. The data have also shown equatorial enhancement in the material distribution.

Our previous studies of the PPN structure independently confirmed (1) equatorially enhanced (toroidal) dust distribution in the innermost region of the shell by mid-IR imaging (Meixner et al. 1999; Ueta et al. 2001), (2) the presence of an elliptical shell surrounding the central torus (Ueta, Meixner, & Bobrowsky 2000) by optical imaging, and (3) an equatorially enhanced hollow spheroid (a combination of the above structures) embedded in a spherically symmetric outer shell would explain all the morphological characteristics by numerical modeling (Meixner et al. 2002). With imaging polarimetry, we have been able to observationally prove that the PPN structure is a hollow spheroid with a built-in equatorial enhancement.

Standard imaging data show only the structure of the circumstellar shells projected to the plane of the sky: the structural information along the line of sight is degenerate. However, the (I_p , P) data set can retain the 3-D properties of these shells because the I_p and P strengths depend on the scattering geometry within the shells. Thus, we can effectively probe the structure of PPNs, by extracting their 3-D information. In addition, we have been able to determine the detailed geometry of our target sources from their polarization properties: *IRAS* 04296 has a quadrupolar shell and does not harbor a disk with collimated outflows and *IRAS* 02229 is oriented in a rather inclined direction with respect to us.

6.2. Morphological Classification Scheme of PPNs

Gledhill et al. (2001) introduced a classification scheme for their imaging polarimetry of PPNs based on the I_p morphology and other polarization properties. These categories are *Shells*, *Bipolars*, and *Core-dominated*. Their study confirmed the SOLE-toroidal vs. DUPLEX-core/elliptical bifurcation found among PPNs and supported the idea that the bifurcation originated from the varying degrees of optical thickness of the shell. Our target PPNs are all *Shells* based on their polarization properties (that is, they are equivalent to SOLE-toroidals). However, our high resolution (I_p , P) data set has

shown a range of morphologies among these *optically thin* PPNs, from a detached shell structure (*IRAS* 07134; Fig. 3b, Fig. 9) to a bipolar cusp structure (*IRAS* 16594; Fig. 7b), and even the mixture of the two (*IRAS* 06530; Fig. 4b, Fig. 10). This suggests that even for *optically thin* PPNs there are multitudes of optical depths that their shells can assume.

As pointed out by Gledhill et al. (2001), the division of the SOLE-DUPLEX bifurcation is not clearly defined. These morphological classes are the both ends of a spectrum in the domain of optical depth. A given PPN can have any optical depth in this continuous distribution of optical depth, and therefore, can assume any morphology along this SOLE-DUPLEX spectrum. The P maps of *IRAS* 02229 and *IRAS* 16594 (Figs. 6c & 7c) have also hinted that inclination angles and highly geometrically thin equatorial density enhancements can leave characteristic signature in the resulting morphology. Thus, we have demonstrated the robustness of our data, and our results further strengthen the suggestion that the optical depth of the shell plays a major role in determining the PPN morphology with an added complexity from the actual geometry of the equatorial enhancement and the inclination of the object. In order to quantitatively understand the PPN morphology in the *optically thin* regime, we need more scattering/polarization models of optically thin shells with consideration of inclination angles.

6.3. Structure of Superwind

PPNs form as a result of stellar mass loss along the AGB (c.f., Kwok 1993; Balick & Frank 2002). The innermost shells are created by stellar material that has been ejected in the most recent mass loss, and thus, represent the latest AGB mass loss history. In other words, the observed shells likely embody the *superwind* shells (Renzini 1981; Iben & Renzini 1983). According to the standard scenario for the AGB mass loss, superwinds are enhanced versions of AGB winds that occur during the final stage of the AGB evolution (corresponding to the thermal pulsing AGB phase; Iben 1995 for a thorough review). Hydrodynamical simulations combined with detailed stellar evolution models have shown that thermal pulses lead to enhanced mass loss events (Schröder, Winters, & Sedlmayr 1999) and the formation of detached dust shells (Steffen, Szczerba, & Schönberner 1998; Steffen & Schönberner 2000). Therefore, we can use the observed shell structure to glimpse the history of superwind mass loss at the end of the AGB phase. Here, we will continue our discussion using *IRAS* 07134 data that shows the density distribution in the greatest detail.

IRAS 07134 has a rather well-defined outer edge at $2''0$ to $2''4$ from the central star as seen in the I and I_p images (Fig. 3a and 3b) and surface brightness profiles (Fig. 9). At the edge, the signal registers at least $10 \sigma_{\text{sky}}$, and hence, the edge is most likely density bounded. The local surface brightness peak at the northern edge of the shell (Fig. 9; i.e., the filamentary structure in the I and I_p maps, Figs. 3a and 3b) likely represents a pile-up of matter at the interface between the faster dust-driven wind and the slower shock-driven wind co-existing in the AGB shell seen in the model calculations (Steffen & Schönberner 2000). Thus, the observed shell in dust-scattered star light very likely embodies the shell created by superwind, especially by the wind associated with the last thermal pulse. Using the distance of 2.4 kpc (Hony et al. 2003) and the wind velocity of 10.5 km s^{-1} (Meixner et al. 2004), the edge represents matter ejected 2000 to 2400 years ago. We also note the presence of inner cavity of about $1''4$

TABLE 5
DYNAMICAL PROPERTIES OF THE SOURCES

Source	Direction	R_{sw} ($''$)	R_{in} ($''$)	D (kpc)	Ref.	v_{exp} (km s^{-1})	Ref.	t_{sw} (yrs)	t_{dyn} (yrs)	Comments
IRAS 07134	Pole (N)	2.2	1.3	2.4	1	10.5	2	990	1430	
	Pole (S)	2.5	1.3 ^a	2.4	1	10.5	2	1300	1430	
	Equator (E)	1.8	0.9	2.4	1	10.5	2	990	990	Prolonged mass loss?
	Equator (W)	2.0	1.3	2.4	1	10.5	2	780	1430	
IRAS 06530	Pole	1.35	0.9 ^b	6.7 ^c	3	14	3	1000	2100	Bipolar cavity
	Equator	0.5	0.35 ^d	6.7 ^c	3	14	3	350	800	Bipolar cusp
IRAS 04296	Extension 1	1.05	0.6	4.0	4	12	5	720	960	Co-existing flows?
	Extension 2	1.75	0.6 ^e	4.0	4	12	5	1800	960	Co-existing flows?
IRAS 02229	Pole	1.05	...	2.2 ^f	6	13	6	850 ^f	0 ^f	
	Equator	0.65	...	2.2 ^f	6	13	6	530 ^f	0 ^f	
IRAS 16594	Pole	1.05	0.6 ^b	2.2	7	16	8	220	1400	Precessing/Rotating Torus
	Equator	1.1	0.7 ^d	2.2	7	16	8	260	460	Bipolar Cusp

REFERENCES. — 1. Hony et al. (2003), 2. Meixner et al. (2004), 3. Hrivnak & Reddy (2003), 4. Meixner et al. (1997), 5. Omont et al. (1993), 6. Reddy, Bakker, & Hrivnak (1999), 7. Van de Steene & van Hoof (2003), 8. Loup et al. (1990)

NOTE. — R_{sw} : superwind shell (I_p) size; R_{in} : inner radius; D : distance; v_{exp} : expansion velocity; t_{sw} : duration of superwind mass loss; t_{dyn} : dynamical expansion time

^a Assumed to be the same as in Pole (N).

^b Estimated from the P profile.

^c 2.8 times as far as *IRAS* 07134, provided the objects have the same luminosity (Hrivnak & Reddy 2003).

^d Measured at $0.''7$ above and below the equatorial plane.

^e Assumed to be the same as in Extension 1.

^f The lower limit.

^g Assuming no cavity.

radius, which is most likely due to the precipitous decrease of mass loss at the end of the AGB phase and defines the *physically detached* nature of the PPN. The width of the superwind shell is about $0.''8$. So, the final mass loss has continued for about 800 years after the edge matter was ejected, and the shell has been expanding for about another 1400 years since the mass loss ceased at the end of the AGB phase. This duration of the final mass loss is consistent with theoretically derived duration of superwind mass loss (Blöcker 1995).

The surface brightness profiles along the equatorial directions are evidence for distinct histories of mass loss experienced by the different equatorial regions of the shell. The observed shell structures suggest that the equatorial density enhancement does not occur symmetrically. There is larger amount of dust grains on the eastern side than the western side. Assuming the constant mass loss velocity of 10.5 km s^{-1} on both sides of the shell, this imbalance could have resulted from prolonged superwind mass loss experienced by the eastern side: while the western superwind terminated about 1400 years ago, the eastern superwind continued another 400 years. Alternatively, the eastern side may not have been moved as far away from the central star as the western side if the wind momentum is equal on both sides.

The presence of the inner cavity confirms the physically detached nature of the shell in *IRAS* 07134. However, other objects do not show the inner cavity as clearly as *IRAS* 07134, especially in I_p . These shells instead show the bipolar cusp structure around the central star. Since the cusp structure suggests the presence of matter in the inner cavity, the presence of the cavity in these shells may not have been seen clearly in I_p as a “hole”. Their P structure is, nevertheless, very similar to that of *IRAS* 07134 (Fig. 4c for *IRAS* 06530, Fig. 5c for *IRAS* 04296, and, Fig. 7c for *IRAS* 16594). Thus, we tentatively suggest their marginally hollow nature. As for the cause of the cusp structure (and the presence of matter in the inner cavity), it is not very clear. However, it may be intrinsic

to PPNs that have optically thicker shells. That is, such cusp structure within the inner cavity may be *required* to form as PPNs develop optically thicker shells. The cusp structure may also be indicative of the presence of a rather flattened torus, which can participate in forming highly elongated shell as we see in these objects. However, the degree to which this shell elongation mechanism works seems to be relatively low in these objects, and thus, these nebulae do not possess the prototypical bipolar morphology.

The presence of a single inner shell in *IRAS* 16594 indicate that the multiple shell structure seen in the optical has been created one elongation at a time while the central region precesses/rotates. However, the quadrupolar structure of *IRAS* 04296 (Fig. 5) suggests two elliptical elongations that can co-exist. Using the distance of 4 kpc (Meixner et al. 1997) and the CO outflow velocity of 12 km s^{-1} , we estimate that the superwind which shaped extension 1 was initiated about 1580 years ago. The absence of the pile-up edges in extension 2 raises an important question about its origin. If the wind velocity along extension 2 is similar to that along extension 1, the wind that shaped extension 2 must have been initiated another 1580 years earlier than the beginning of extension 1 formation. If the shaping of extension 2 was initiated about the same time as the shaping of extension 1 by the onset of superwind, the wind velocity along extension 2 must have been about 24 km s^{-1} . If the amount of dust in the two extensions is different (e.g. Sahai 1999), two winds with the same velocity could generate elongations with differing length. Either case, two elongations seem to have been generated concurrently at least for some time. Thus, there are likely multiple channels to create multi-polar shell structures.

The polarimetric data have shown that the presence of equatorial density enhancement is prevalent among PPNs with widely varying degrees of strength. With the presence of axisymmetry in the late AGB mass loss history being established as fundamental, it is then reasonable to assume

that something equally fundamental is responsible as the origin for axisymmetry - the equatorial enhancement - in the AGB mass loss. An axisymmetric mass loss process may be a natural consequence of very fundamental physics involved in any stellar mass loss and/or any dusty outflowing astronomical phenomena. In Table 5, we summarize quantities of geometric and dynamic nature of the objects. We measured the inner and superwind (outer) radii (R_{in} and R_{sw} , respectively) assuming the presence of the inner cavity based on their P structure. Using the distance and shell expansion velocities for these objects taken from the literature (Loup et al. 1990; Omont et al. 1993; Meixner et al. 1997; Reddy, Bakker, & Hrivnak 1999; Hony et al. 2003; Hrivnak & Reddy 2003; Van de Steene & van Hoof 2003; Meixner et al. 2004), we derived the duration of superwind (T_{sw}) and expansion the cessation of mass loss (t_{dyn}). These quantities would not only characterize the axisymmetric nature of PPNs but also serve as constraining parameters for any models to generate equatorial enhancements in the AGB mass loss with magnetic fields/companion objects (e.g., Soker 1998; Mastrodemos & Morris 1999; Matt et al. 2000).

7. CONCLUSIONS

We have performed imaging polarimetry using *HST*/NICMOS to observe optically thin PPNs, with the aim to reveal their density structure by the polarized intensity, I_p . In the optically thin regime, the (I_p , P) data set can effectively probe the presence of scattering bodies distributed in the vicinity of the bright central illumination source. This is a great advantage of imaging polarimetry over conventional imaging, in which the central star (and its PSF structure) will always dominate in these objects and the detection of faint nebulosities will not be trivial.

We have found that (1) *IRAS* 07134 is an equatorially enhanced, prolate hollow spheroidal shell that is nearly edge-on. The presence of the inner cavity has been observationally confirmed and the peak imbalance seen in the present study and past study of mid-IR dust emission has been determined to be due to density effects, (2) *IRAS* 06530 is a prolate spheroid with a possible cavity, but its equatorial enhancement is more bipolar-like, filling the cavity with some

matter, (3) *IRAS* 04296 is a combination of two spheroids intersecting with each other with one of the extensions being inclined towards us, (4) *IRAS* 02229 resembles *IRAS* 06530, but has greater equatorial enhancement and the inclination angle closer to pole-on compared with other objects, and (5) *IRAS* 16594 has very bipolar-like morphological characteristics indicating relatively high optical depth of the shell, whose multi-polar structure is due to a pair of outflows channeled out from a rotating/precessing torus. These observations have also indicated that there are multiple channels of evolution for multi-polar shells: while *IRAS* 04296 seems to be a co-existing quadrupolar nebula, multiple poles of *IRAS* 16594 likely result from a rotating/precessing torus.

Our observations have strongly suggested that PPNs do possess an inner cavity which physically separates the shell from the central star and represents dynamical time for the shell expansion since the end of the AGB phase. The inner PPN shell seems to be density bounded and its structure is likely shaped by superwind. In the case of *IRAS* 07134, we have been able to observationally confirm that the inner PPN structure is a hollow spheroid with some equatorial enhancement. We have also confirmed that SOLE-toroidal PPNs have optically thin shells and that the varying degree of equatorial density enhancement (i.e., the optical depth) determines the detailed shell morphology even among this specific group of optically thin PPNs.

This research is based on observations with the NASA/ESA Hubble Space Telescope, obtained at the Space Telescope Science Institute (STScI), which is operated by the Association of Universities for Research in Astronomy, Inc. under NASA contract No. NAS 5-26555. Authors have been supported by NASA STI 9377.05-A. Ueta has also been supported by the project IAP P5/36 financed by FSTC of the Belgian State. The assistance from E. Roye and A. Schultz during data reduction was appreciated. We thank K. Volk who generously provided us with mid-IR data taken at Gemini. F. Courbin is also thanked for his help using the MCS deconvolution software. We also appreciate valuable comments from anonymous referee that helped improving the paper.

REFERENCES

- Balick, B., & Frank, A. 2002, *ARA&A*, 40, 439
 Blöcker, T. 1995, *A&A*, 297, 727
 Dayal, A., Hoffmann, W. F., Biegging, J. H., Hora, J. L., Deutsch, L. K., & Fazio, G. G. 1998, *ApJ*, 492, 603
 Dickinson, M., et al. 2002, in "HST NICMOS Data Handbook Version 5.0", ed. B. Mobasher (Baltimore: STScI)
 García-Hernández D. A., Manchado, A., García-Lario, P., Benítez Cañete, A., Acosta-Pulido, J. A., Pérez García, A. M. 2004, in *ASP Conf. Ser. Vol. 313, Asymmetric Planetary Nebulae III*, eds. M. Meixner, J. Kastner, B. Balick, & N. Soker (San Francisco: ASP), 367
 Gledhill, T. M., Chrysostomou, A., Hough, J. H., & Yates, J. A. 2001, *MNRAS*, 322, 321
 Gledhill, T. M., & Takami, M. 2001, *MNRAS*, 328, 266
 Gledhill, T. M., & Yates, J. A. 2003, *MNRAS*, 343, 880
 Hines, D. C., Schmidt, G. D., & Schneider, G. 2000, *PASP*, 112, 983
 Hony, S., Tielens, A. G. G. M., Waters, L. B. F. M., & de Koter, A. 2003, *A&A*, 402, 211
 Hrivnak, B. J., & Kwok, S. 1999, *ApJ*, 513, 869
 Hrivnak, B. J., & Reddy, B. E. 2003, *ApJ*, 590, 1049
 Hrivnak, B. J., Kwok, S., & Su, K. Y. L. 1999, *ApJ*, 524, 849
 Iben, I. Jr. 1981, *ApJ*, 246, 278
 Iben, I. Jr. 1995, *Physics Report*, 250, 2
 Iben, I. Jr., & Renzini, A. 1983, *ARA&A*, 21, 271
 Jura, M., Chen, C., & Werner, M. W. 2000, *ApJ*, 544, L141
 Koekemoer, A. M., et al. 2002, "HST Dither Handbook", Version 2.0 (Baltimore: STScI)
 Kwok, S. 1993, *ARA&A*, 31, 63.
 Kwok, S., Su, K. Y. L., & Hrivnak, B. J. 1998, *ApJ*, 501, L117
 Kwok, S., Volk, K., & Hrivnak, B. J. 2002, *ApJ*, 573, 720
 Loup, C., Forveille, T., Nyman, L. Å., & Omont, A. 1990, *A&A*, 227, L29
 Magain, P., Courbin, F. and Sohy, S. 1998, *ApJ*, 494, 472
 Malhotra, S., et al. 2002, "NICMOS Instrument Handbook", Version 5.0 (Baltimore: STScI)
 Mastrodemos, N. & Morris, M. 1999, *ApJ*, 523, 357
 Matt, S., Balick, B., Winglee, R., & Goodson, A. 2000, *ApJ*, 545, 965
 Meixner, M., Ueta, Bobrowsky, M., & Speck, A. K. 2002, *ApJ*, 571, 936
 Meixner, M., Ueta, T., Dayal, A., Hora, J. L., Fazio, G., Hrivnak, B. J., Skinner, C. J., Hoffmann, W. F., & Deutsch, L. K. 1999, *ApJS*, 122, 221
 Meixner, M., Skinner, C. J., Graham, J. R., Keto, E., Jerrigen, J. G., & Arens, J. F. 1997, *ApJ*, 482, 897
 Meixner, M., Zalucha, A., Ueta, T., Fong, D., & Justtanont, K. 2004, *ApJ*, accepted
 Omont, A., Loup, C., Forveille, T., te Lintel Hekkert, P., Habing, H., & Sivagnanam, P. 1993, *A&A*, 267, 515
 Reddy, B. E., Bakker, E. J., & Hrivnak, B. J. 1999, *ApJ*, 524, 831
 Renzini, A. 1981, in *Physical Processes in Red Giants*, eds. I. Iben Jr. & A. Renzini (Dordrecht: Reidel), 431
 Sahai, R. 1999, *ApJ*, 524, L125
 Schröder, K.-P., Winters, J. M., & Sedlmayr, E. 1999, *A&A*, 349, 898

- Soker, N. 1998, MNRAS, 299, 1242
Sparks, W. B., & Axon, D. J. 1999, PASP, 111, 1298
Steffen, M., & Schönberner, D. 2000, A&A, 357, 180
Steffen, M., Szczerba, R., & Schönberner, D. 1998, A&A, 337, 149
Su, K. Y. L., Hrivnak, B. J., & Kwok, S. 2001, AJ, 122, 1525
Su, K. Y. L., Hrivnak, B. J., Kwok, S., & Sahai, R. 2003, AJ, 126, 848
Ueta, T., & Meixner, M. 2003, ApJ, 586, 1338
Ueta, T., Meixner, M., & Bobrowsky, M. 2000, ApJ, 528, 861
Ueta, T., Meixner, M., Hinz, P. M., Hoffmann, W. F., Brandner, W., Dayal, A., Deutsch, L. K., Fazio, G. G., & Hora, J. L. 2001, ApJ, 557, 831
Ueta, T., Meixner, M., Moser, D. E., Pyzowski, L. A., & Davis, J. S. 2003, AJ, 125, 2227
Ueta, T., de Vlieger, M., Van de Steene, G. C., Szczerba, R., & Van Winckel, H. 2004, A&A, submitted
Van de Steene, G. C., & van Hoof, P. A. M. 2003, A&A, 406, 773
Van Winckel, H. 2003, ARA&A, 41, 391
Whitney, B. A., & Hartmann, L. 1993, ApJ, 402, 605